# Seismic scattering and absorption parameters in the W-Bohemia/Vogtland region from elastic and acoustic radiative transfer theory

Peter J. Gaebler, Tom Eulenfeld and Ulrich Wegler

*BGR Federal Institute for Geosciences and Natural Resources, Stilleweg 2, D-30655 Hannover, Germany. E-mail: Peter.Gaebler@bgr.de*

## SUMMARY

In this study, frequency-dependent seismic scattering and intrinsic attenuation parameters for the crustal structure beneath the W-Bohemia/Vogtland swarm earthquake region close to the border of Czech Republic and Germany are estimated. Synthetic seismogram envelopes are modelled using elastic and acoustic radiative transfer theory. Scattering and absorption parameters are determined by fitting these synthetic envelopes to observed seismogram envelopes from 14 shallow local events from the October 2008 W-Bohemia/Vogtland earthquake swarm. The two different simulation approaches yield similar results for the estimated crustal parameters and show a comparable frequency dependence of both transport mean free path and intrinsic absorption path length. Both methods suggest that intrinsic attenuation is dominant over scattering attenuation in the W-Bohemia/Vogtland region for the investigated epicentral distance range and frequency bands from 3 to 24 Hz. Elastic simulations of seismogram envelopes suggest that forward scattering is required to explain the data, however, the degree of forward scattering is not resolvable. Errors in the parameter estimation are smaller in the elastic case compared to results from the acoustic simulations. The frequency decay of the transport mean free path suggests a random medium described by a nearly exponential autocorrelation function. The fluctuation strength and correlation length of the random medium cannot be estimated independently, but only a combination of the parameters related to the transport mean free path of the medium can be computed. Furthermore, our elastic simulations show, that using our numerical method, it is not possible to resolve the value of the mean free path of the random medium.

**Key words:** Inverse theory; Coda waves; Seismic attenuation; Wave scattering and diffraction; Wave propagation; Europe.

## 1 INTRODUCTION

As seismic waves propagate through the Earth's heterogeneous subsurface, they lose energy on their way from source to receiver. This loss of energy implies a decrease in amplitude of the seismic wave and is mainly influenced by three factors. The first factor is the spherical divergence or geometrical spreading. Seismic energy, when emitted from a point like source, spreads out in form of a spherical wave front. In a homogeneous medium the energy density at any point of the wave front $E(r)$ is proportional to $1/r^2$, where $r$ is the distance from the source. As the amplitude of the seismic wave equals $\sqrt{E(r)}$, it must decrease with $1/r$ for energy to be conserved. The second reason for a decrease in seismic wave amplitude is intrinsic attenuation. As the propagation of seismic energy is not completely elastic, small fractions of energy are continuously converted to different forms of energy, for example, frictional heat or mineral dislocations. A third quantity, the scattering attenuation,

can additionally cause a decrease in wave amplitude and contributes to the total attenuation of seismic waves (Aki 1981; Toksöz *et al.* 1988). Scattering attenuation can be described as the redistribution of energy at 3-D-heterogeneities in the subsurface. These scattering events are the cause for the generation of the seismic coda signal, recorded after the passage of the primary seismic waves (Aki 1969; Aki & Chouet 1975).

The decay of the high-frequency seismic coda signal is related to the local properties of the subsurface (Trégourès *et al.* 2002). The investigation and modelling of the decay can therefore be used to investigate local physical properties of the underground, such as intrinsic and scattering attenuation (Abubakirov & Gusev 1990; Lacombe *et al.* 2003).

Several techniques are described to model the high-frequency seismic wave field and to investigate and separate the two parameters of intrinsic and scattering attenuation. One possible approach to investigate the attenuation parameters is the diffusion

approximation (Dainty *et al.* 1974; Wegler & Lühr 2001). This approach is based on the assumption of strong multiple scattering and is only valid for long lapse times. Another possible approach to investigate the attenuation parameters is the multiple lapse time window analysis (MLTWA; Fehler *et al.* 1992), which employs the coda normalization method (CNM) according to Aki (1980). For studies using MLTWA see, for example, Hoshiba (1993) and Carolé & Sato (2010). MLTWA is based on radiative transfer theory (RTT), a further suitable method to describe the propagation of seismic energy in a scattering medium. RTT was first introduced by Chandrasekhar (1960) to describe the transport of light in the turbulent atmosphere and was only later transferred to the field of seismology (Weaver 1990; Turner & Weaver 1994; Ryzhik *et al.* 1996). Many studies based on RTT make use of the approach of isotropic acoustic scattering of seismic energy to separate intrinsic and scattering attenuation. This method only treads the propagation of *S*-energy under the assumption of scattering events with no preferred scattering direction. For isotropic, acoustic RTT in full space exact analytical solutions to the transport problem exist (Zeng *et al.* 1991). The assumption of anisotropic scattering (Gusev & Abubakirov 1987; Wegler *et al.* 2006) is a further development in the RTT approach. This assumption allows to include forward scattering in the simulations and therefore enables the possibility of modelling the peak broadening of the direct seismic wave arrivals. Further studies model the propagation of elastic energy (Zeng 1993; Margerin *et al.* 2000; Przybilla *et al.* 2006; Przybilla & Korn 2008) and therefore include the simulation of *P*-energy, as well as conversions between the two states of energy. The propagation of elastic energy assuming multiple anisotropic scattering in a continuous random medium with a deterministic background structure is, for example, described by Sens-Schönfelder *et al.* (2009) and Gaebler *et al.* (2015). This approach allows to model the entire seismogram envelope in a realistic model setup, including interfaces and the free surface condition. In the RTT simulations only high-frequency body waves are considered. Furthermore wave phenomena, such as dispersion, superposition or interference, are not included in this theory.

In this study we focus on the estimation of *S*-wave scattering and intrinsic attenuation parameters with the aim to obtain information about the small scale heterogeneities of the medium. The two methods used for the computation of synthetic seismogram envelopes are described in Section 2. The study area, including station and event details, as well as the generation of the observed seismogram envelopes, is presented in Section 3. Section 4 describes the process of generating the elastic and acoustic forward envelopes, as well as the analysis of the synthetic data. The results of the estimation of intrinsic and scattering attenuation are given in Section 5.1. Furthermore, results concerning parameter trade-offs and resolution limits of the parameters are described in Section 5.2. The outcomes of this study are discussed and concluded in Sections 6 and 7.

## 2 METHODS

The crustal scattering and intrinsic attenuation parameters are estimated by comparing observed envelopes with synthetic envelopes calculated using two different approaches, both based on the radiative transfer of seismic energy. The first method assumes multiple anisotropic scattering of elastic energy at randomly distributed small-scale heterogeneities and is explained in Section 2.1. The second approach models the transport of acoustic energy under the assumption of multiple isotropic scattering and is introduced in Section 2.2.

### 2.1 Elastic radiative transfer theory

The first approach is based on the elastic transport of seismic energy and features multiple anisotropic scattering of seismic energy in a continuous random medium with a deterministic background structure. The algorithm does not only model the propagation of *S*-energy, but additionally allows to simulate the transfer of *P*-energy, as well as conversions between these two forms of energy. The random heterogeneities of the medium are described by an exponential autocorrelation function (ACF), the deterministic background structure is represented by a layer over half space model with a free surface condition. This setup represents the crustal lithosphere overlying the mantle. The solutions to the elastic radiative transfer equations (RTE) are based on a numerical Monte Carlo (MC) method, which can be referred to as a particle counting method (Gusev & Abubakirov 1987; Yoshimoto 2000). The central quantity of the RTEs, the specific intensity *I*, which describes the flux of energy, is modelled by a number density of particles. These particles are emitted from a source with an isotropic radiation pattern with a fixed ratio of radiated *P*- and *S*-energy (Shearer 1999; Sato *et al.* 2012). During the simulation, particles can experience scattering processes at medium heterogeneities following the Born approximation (Sato *et al.* 2012). These scattering events include mode conversions and changes in propagation direction of the particle. In contrast to the theory of isotropic scattering, the anisotropic approach includes the more realistic assumption of forward scattering. Particles lose energy as they propagate through the medium to account for intrinsic attenuation. When no scattering events occur, the general particle propagation is governed by ray theory. This includes the interaction with interfaces (reflections, transmissions and mode conversions), as well as ray bending in regions with velocity gradients. The particle energy is recorded in finite volumes around the receiver elements in consecutive time steps. This results in 4-D-snapshots of the seismic energy, consisting of three spatial and one temporal dimension. Snapshots contain recordings of *P*- and *S*-energy, as well as records of multi-component translational motions in different coordinate systems. In this study, we use the ray-based *LQT*-coordinate system for the recording of the particles. For a detailed description of the modelling algorithm we refer the reader to Sens-Schönfelder *et al.* (2009), for information on the modelling of the multi-component envelopes and the choice of the recording system see Gaebler *et al.* (2015).

### 2.2 Acoustic radiative transfer theory

The second approach used for the computation of the synthetic envelopes employs acoustic RTT. In the acoustic theory only one mode of energy is modelled. As *S*-energy dominates the seismic signal from the first arrival of the direct *S*-wave until the late parts of the seismic coda (Ryzhik *et al.* 1996; Hennino *et al.* 2001; Gaebler *et al.* 2015), only the propagation of *S*-energy is simulated. The transfer of *P*-energy and mode conversions are ignored. Furthermore we assume a homogeneous background velocity in the model. For these assumptions an exact radiative transfer solution for the energy density is provided by Zeng *et al.* (1991) for a full space model. For simplicity, the analytic approximate solution by Paasschens (1997) is used, which is an interpolation of the exact solutions for the 2-D- and 4-D-case. According to Paasschens (1997) the deviation of the approximate solution used in this study from the exact solution (Zeng *et al.* 1991) is below five per cent. Larger perturbations only occur in the tail of the direct *S*-wave. For purposes of this study these deviations are acceptable. Pulse broadening of the *S*-wave, due

to reverberations in the crustal layer and velocity fluctuations, is not included in the modelling. The ballistic *S*-waves are only represented by a delta peak in the acoustic simulations. To account for these systematic differences in the shape of the direct *S*-envelope, an average value around this peak is calculated to describe the total energy content of the *S*-wave onset (Sens-Schönfelder & Wegler 2006). The length of the time window used to calculate the average *S*-wave amplitude is 2 s. The energy in this time window mainly consists of unscattered energy, which is described correctly in our approximation. We include a correction factor of four to account for the free surface condition (Emoto *et al.* 2010). The final modelled energy density $E(\mathbf{r}, t)$ is given by:

$$E(\mathbf{r}, t) = 4WRG(\mathbf{r}, t)\mathrm{e}^{-bt}. \tag{1}$$

$W$ represents a source energy term, $R$ is the site response at the receiver, $G(\mathbf{r}, t)$ is the energy density Green's function in full space (Sato *et al.* 2012) and $r$ is the distance from the source. Intrinsic attenuation is accounted for by multiplication with a time-dependent factor of the form $\mathrm{e}^{-bt}$, with $b$ being the absorption coefficient defined as:

$$b = \frac{2\pi f}{Q_S^i}. \tag{2}$$

$f$ is the centre frequency and $Q_S^i$ is the intrinsic quality factor for *S*-waves. A combined grid search and inversion process of the individual events in the different frequency bands is used to estimate crustal scattering parameters in terms of the transport scattering coefficient $g^*$ and the intrinsic attenuation in form of the absorption coefficient $b$. Furthermore station site responses $R$ and source radiation energies $W$ are simultaneously computed during the estimation process.

# 3 STUDY AREA, DATA AND OBSERVED ENVELOPES

Our investigations on scattering and intrinsic attenuation parameters focus on the crustal structure beneath the W-Bohemia/Vogtland region, situated at the border of the Czech Republic and Germany (Fig. 1). This region is attributed to the western part of the Bohemian Massif. The main tectonic structures in this area are the Eger-Rift-system (Prodehl *et al.* 2006) and the Regensburg–Leipzig–Rostock zone with the Cheb basin in the centre. Numerous faults of various striking directions can be found in the area, with the most prominent being the Márianské Lázně fault (Fischer *et al.* 2013). The study area is of high interest as it is one of the few intra-continental regions in Europe that exhibits present activity of geodynamical processes. Hints for this processes include the natural degassing of $CO_2$ from great depths that is visible in the form of $CO_2$ rich mineral waters or in the existence of wet and dry mofettes (Weinlich *et al.* 2003; Geissler *et al.* 2005). Another hint to the geodynamic processes is the present seismic activity in the W-Bohemia/Vogtland region. This activity mainly occurs in earthquake swarms with magnitudes up to 5 ($M_L$). The most recent swarms occurred in January 1997, August to December 2000, October to November 2008, October 2010, August to September 2011 and in August 2014. The earthquake swarms have been subject to numerous studies (Heinicke *et al.* 2009; Vavryčuk 2011). The underlying triggering mechanism of the earthquakes is still under debate. For more information about the study area, the swarm earthquakes and the possible triggering mechanisms we refer the reader to the review paper by Fischer *et al.* (2013).
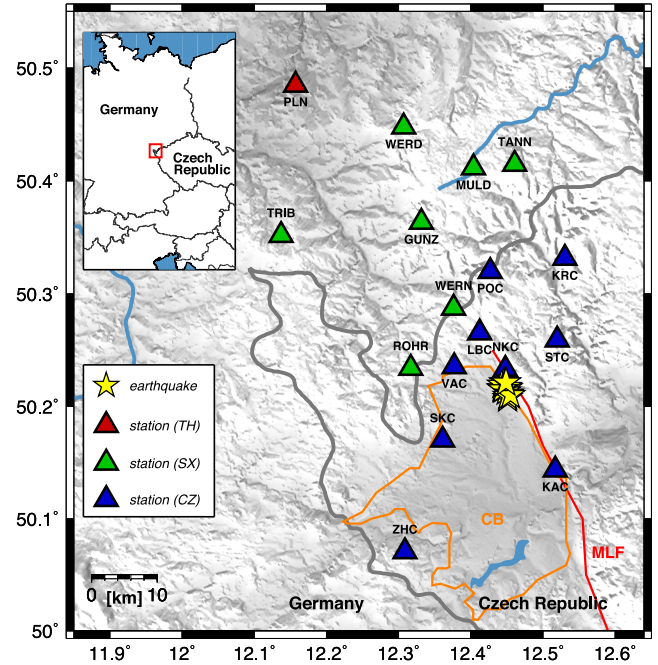


**Figure 1.** Map of the study area showing the W-Bohemia/Vogtland region in the western part of Czech Republic, close to the German border. Coloured triangles indicate seismic stations from different networks (TH, SX, CZ). The investigated local swarm earthquakes are indicated by yellow stars. Grey background shading represents topography. The Márianské Lázně fault (MLF) is indicated by the red line, the orange line confines the location of the Cheb basin (CB). For additional details on earthquakes and stations see also Tables 1 and 2.

Data from 14 earthquakes from the October 2010 earthquake swarm is used. Magnitudes ($M_L$) of the earthquakes are in the range from 3.1 to 4.2, event depths vary between 10 and 12 km. Earthquake locations, event depths, magnitudes and source times were estimated by the German Seismological Central Observatory. For an illustration of the epicentre locations see Fig. 1, event details are given in Table 1. The events are recorded at 17 three-component, broad-band seismic stations, seven operated by the Saxon seismic network (SX), nine by the Czech WEBNET network (CZ) (Horálek *et al.* 2000) and one operated by the Thuringian seismic network (TH). A list of stations is given in Table 2, station locations for the different networks are illustrated in Fig. 1.

This choice of stations and earthquakes results in hypocentral distances from 10 km up to around 40 km. Accordingly, travel times range from as low as 2 s for *P*-waves to 14 s for *S*-waves. *P*- and *S*-wave arrivals were manually picked. From these travel times a simple average velocity model for this region was calculated with $v_P = 5.12 \text{ km s}^{-1}$ and $v_S = 3.12 \text{ km s}^{-1}$. The estimated seismic velocities are used as crustal seismic velocities in the computation of the synthetic seismogram envelopes.

The forward simulations of the elastic and acoustic RTT approaches (Section 4) are compared to observed real data seismogram envelopes. These are generated by processing three-component broadband data from the 14 events given in Table 1 recorded at the stations listed in Table 2. For the comparison with the synthetic data, the seismograms were filtered using a two-corner Butterworth filter with zero shift in four frequency bands: 2–4, 4–8, 8–16 and 16–32 Hz. This results in centre frequencies of 3, 6, 12 and 24 Hz. Data was demeaned and detrended prior to filtering. After filtering, seismogram envelopes are computed using the Hilbert

**Table 1.** Swarm earthquakes from the W-Bohemia/Vogtland region used in this study.

| # | Source time (UTC) | Coordinates | Depth | Mag |
|---|---|---|---|---|
| 01 | 2008-10-10 00:39:44 | 50.215°N 12.445°E | 11 km | 3.6 ($M_L$) |
| 02 | 2008-10-10 03:22:04 | 50.216°N 12.443°E | 12 km | 3.9 ($M_L$) |
| 03 | 2008-10-10 04:22:16 | 50.221°N 12.446°E | 12 km | 3.1 ($M_L$) |
| 04 | 2008-10-10 07:32:01 | 50.216°N 12.451°E | 11 km | 3.3 ($M_L$) |
| 05 | 2008-10-10 08:08:45 | 50.213°N 12.449°E | 11 km | 4.2 ($M_L$) |
| 06 | 2008-10-10 11:18:41 | 50.217°N 12.450°E | 11 km | 3.5 ($M_L$) |
| 07 | 2008-10-10 19:08:31 | 50.219°N 12.443°E | 11 km | 3.3 ($M_L$) |
| 08 | 2008-10-12 07:44:15 | 50.207°N 12.451°E | 11 km | 3.9 ($M_L$) |
| 09 | 2008-10-14 04:01:35 | 50.215°N 12.444°E | 12 km | 3.2 ($M_L$) |
| 10 | 2008-10-14 19:00:32 | 50.211°N 12.453°E | 12 km | 4.0 ($M_L$) |
| 11 | 2008-10-21 02:14:01 | 50.221°N 12.448°E | 11 km | 3.4 ($M_L$) |
| 12 | 2008-10-28 08:30:10 | 50.209°N 12.451°E | 11 km | 4.1 ($M_L$) |
| 13 | 2008-10-28 10:07:00 | 50.210°N 12.444°E | 10 km | 3.1 ($M_L$) |
| 14 | 2008-10-28 14:51:52 | 50.221°N 12.449°E | 11 km | 3.1 ($M_L$) |

**Table 2.** Seismic stations used in this study.

| Network | Station | Coordinantes | Elevation | Location |
|---|---|---|---|---|
| SX | ROHR | 50.234°N 12.317°E | 629 m | Rohrbach |
| SX | WERN | 50.287°N 12.376°E | 672 m | Wernitzgrün |
| SX | GUNZ | 50.364°N 12.332°E | 669 m | Gunzen |
| SX | MULD | 50.412°N 12.404°E | 678 m | Muldenberg |
| SX | TANN | 50.415°N 12.461°E | 836 m | Tannbergsthal |
| SX | TRIB | 50.352°N 12.137°E | 510 m | Obertriebel |
| SX | WERD | 50.448°N 12.307°E | 589 m | Werda |
| CZ | NKC | 50.233°N 12.448°E | 564 m | Nový Kostel |
| CZ | VAC | 50.235°N 12.377°E | 530 m | Vackov |
| CZ | LBC | 50.266°N 12.412°E | 638 m | Luby |
| CZ | STC | 50.259°N 12.520°E | 666 m | Studenec |
| CZ | SKC | 50.170°N 12.361°E | 455 m | Skalná |
| CZ | KAC | 50.144°N 12.517°E | 524 m | Kaceřov |
| CZ | POC | 50.320°N 12.427°E | 790 m | Počátky |
| CZ | KRC | 50.332°N 12.530°E | 760 m | Kraslice |
| CZ | ZHC | 50.071°N 12.309°E | 631 m | Zelená Hora |
| TH | PLN | 50.485°N 12.157°E | 432 m | Plauen |

transformation. The resulting traces are comparable to the energy envelopes of the synthetic data created with the elastic and acoustic approach. Noise is removed from the traces by subtracting the average level of noise in a 2 s time window prior to the arrival of the first direct wave. In the acoustic case the three-component envelopes are stacked to obtain total energy envelopes. For comparisons with the elastic simulations, the observed traces are rotated from the classical *ZNE*-system into the ray-based *LQT*-coordinate system prior to the computation of the Hilbert envelopes. After stacking, respectively rotation, the envelopes are smoothed with a 0.5 s time window to account for different realizations of the medium. This is necessary, as the observed data envelopes only account for one single medium realization, while the RTT simulations on the other hand represent an ensemble average. The final step of the processing of the elastic simulations includes a correction for site effects at the stations using the CNM according to Aki (1980). A coda normalization is not required in the acoustic approach, as site effects are determined during the inversion process.

## 4 FORWARD SIMULATIONS AND ANALYSIS

For the elastic RTT forward simulations (Section 2.1) the multi-component envelopes are recorded in the ray based *LQT*-system in a model domain with lateral dimensions of $100 \times 100$ km, which spec-

ify the model extent in north-south and east-west direction. Energy is only recorded in the model domain, but the particle propagation is modelled throughout the entire time interval, irrespective of particle position. Particles outside the recording domain can, for example, be backscattered and therefore contribute to the recorded energy. The receiver volumes have the dimensions of $0.5 \times 0.5 \times 0.5$ km. The seismic source is placed in the centre of the model in a depth of 11.2 km, which is the average depth of the used swarm earthquakes (Table 1). Small differences in event depth compared to the used average depth do not influence the synthetic envelopes from the elastic simulations significantly. We use a source with an isotropic radiation pattern with a fixed ratio of radiated *P*- to *S*-energy of ∼0.05 (Shearer 1999). The dimensions of the recording domain and the placement of the source allow the simulation of envelopes in epicentral distances up to 50 km. In the simulations we use a layer over half space model, with the layer representing the crust with a thickness of 30 km (Zeis *et al.* 1990). The half space represents the mantle. The crustal scattering and intrinsic attenuation parameters are estimated in different frequency bands and for each individual earthquake. A grid search approach is used to find the parameters, which result in synthetic envelopes that best describe the observed traces. Source energies for the individual events are calculated during the grid search process. For predefined sets of crustal parameters of intrinsic and scattering attenuation, the forward simulations are computed in the different frequency bands. The scattering is expressed through the parameters of density and velocity root mean square fractional fluctuations $\epsilon$ of the medium, further referred to as fluctuation strength, through the correlation length $a$ and through the type of the random medium. The fractional fluctuations $\epsilon$ for the wave velocities $v_P$ and $v_S$ are equal and are correlated to the density of rocks according to following equation following Birch's law (Birch 1961):

$$\epsilon(\mathbf{x}) = \frac{\delta v_P(\mathbf{x})}{v_P} = \frac{\delta v_S(\mathbf{x})}{v_S} = \frac{1}{\nu} \frac{\delta \rho(\mathbf{x})}{\rho^0}. \quad (3)$$

$v_P$, $v_S$ are the average background velocities for *P*- and *S*-waves, $\rho$ represents the average background density. $\delta v_P$, $\delta v_S$ and $\delta \rho$ indicate deviations from the average background velocities, respectively background density. The parameter $\nu$ links the fluctuations of velocities and density to one common parameter $\epsilon$ and ranges between 0.78 and 0.8 for typical crustal lithosphere (Sato *et al.* 2012). Here we use a fixed value of $\nu = 0.8$. Scattering direction is dependent on the value $a$, as well as on the wavenumber $k$. For small wavenumbers (low frequencies, $ak_S \ll 1$) scattering becomes wide angle scattering, for large wavenumbers (high frequencies, $ak_S \gg 1$)

scattering in the forward direction becomes dominant (Sato *et al.* 2012). Different values of $\epsilon$ and $a$ lead to different values for the transport mean free path, which is a measure of scattering strength. Intrinsic attenuation is expressed through the quality factor $Q^i$. The parameters are chosen to uniformly sample a parameter space of realistic crustal scattering and absorption values (Sato *et al.* 2012). Fluctuation strength $\epsilon$ varies in the range from 0.1 to 10 per cent, the correlation length $a$ is chosen to be equally sampled between 0.1 and 10 km. The random medium is described by an exponential ACF. The intrinsic attenuation for *S*-waves $Q_S^i$ varies between 100 and 1500, which transfers to values for the intrinsic quality factor for *P*-waves $Q_P^i$ of 225 to 3375 assuming a fixed $Q_P^i/Q_S^i$ ratio of 2.25 (Shearer 1999). The scattering and intrinsic attenuation parameters in the mantle are set to equal the crustal values in the predefined parameter sets. To ensure reflections at the interface between crust and mantle, wave speeds in the mantle are set to 6.4 km s$^{-1}$ for *P*-waves and to 3.6 km s$^{-1}$ for *S*-waves . The influence of scattering and intrinsic attenuation in the mantle on the propagation of seismic waves in a local frame is weak (Gaebler *et al.* 2015), which justifies our choice of fixed mantle parameters. For each of the individual earthquakes in the different frequency bands the pre-computed forward simulations can now be used to find the best fitting set of crustal parameters to describe the observed data.

The acoustic forward simulations are calculated according to the method described in Section 2.2. The best fitting parameters are estimated by inverting the observed envelopes. In the acoustic simulations the scattering strength is expressed through the transport scattering coefficient $g^*$ or through the scattering coefficient $g^0$, which are equal in the acoustic approximation ($l^* = l^0$). Intrinsic attenuation is expressed through the absorption coefficient $b$ (eq. 2).

The fit of the forward simulations with respect to the observed envelopes is evaluated in terms of its misfit. The misfits are calculated as the sample-wise logarithmic L2-norm. Using logarithmic differences ensures that the high-amplitude direct wave and the lower-amplitude coda values have a similar weight in the misfit calculation.

To compare the absorption results of both the acoustic and elastic method, the intrinsic attenuation will further be presented as the absorption path length for *S*-waves, $l_S^i$ defined as:

$$l_S^i = \frac{v_S}{b} = \frac{v_S Q_S^i}{2\pi f}. \tag{4}$$

The scattering strength will further be expressed through the transport mean free path for *S*-waves $l_S^*$, which can be regarded as the propagation distance required for a wave to lose memory of its initial direction. In the elastic case the scattering properties are represented by the density and velocity fluctuations $\epsilon$ and the correlation length $a$. The parameters $\epsilon$ and $a$ are linked to the transport mean free path $l_S^*$ via the total scattering coefficients $g_{ij}$ and the Fourier spectra of the ACF of the medium (Sato *et al.* 2012). The elastic transport mean free path for *S*-waves $l_S^*$ is given as (Przybilla *et al.* 2009):

$$l_{S,e}^* = \frac{g_{PS}^0 + g_{PP}^0 - g_{PP}^D + g_{SP}^D}{(g_{PS}^0 + g_{PP}^0 - g_{PP}^D)(g_{SP}^0 + g_{SS}^0 + -g_{SS}^D) - g_{PS}^D g_{SP}^D}. \tag{5}$$

Here subscripts *P* and *S* denote the two possible modes of energy, *PS*, for example, denotes the scattering from *P*- to *S*-energy. The terms $g_{ij}^0$ and $g_{ij}^D$ are defined, according to Sato *et al.* (2012), as:

$$g_{ij}^0 = \frac{1}{4\pi} \oint g_{ij}(\theta, \phi) d\Omega, \tag{6}$$

$$g_{ij}^D = \frac{1}{4\pi} \oint g_{ij}(\theta, \phi) \cos\theta d\Omega. \tag{7}$$

Under the assumption of isotropic scattering the transport mean free path $l_S^*$ is equal to the mean free path of *S*-waves $l_S^0$. In the acoustic simulations the total scattering coefficient $g_0$ is estimated, which is related to the transport mean free path by:

$$l_{S,a}^* = \frac{1}{g_0} = \frac{1}{g^*}. \tag{8}$$

## 5 RESULTS

In Section 5.1 the results of the estimation of scattering and absorption parameters of the crustal structure are presented. Investigations of parameter trade-offs and limits in the resolution possibilities of the parameters are discussed in Section 5.2.

### 5.1 Separation of intrinsic and scattering attenuation

The crustal scattering and intrinsic attenuation parameters are estimated by comparisons of elastic and acoustic synthetic RTT envelopes to observed data envelopes. An example of the envelopes for one individual earthquake from the elastic and acoustic approach, that best describe the observed envelopes is shown in Fig. 2.

The observed envelopes in Fig. 2 are created from earthquake 10 (Table 1) in the frequency band from 4 to 8 Hz ($f_c = 6$ Hz). Here we only show recordings from five exemplary stations (LBC, ROHR, KRC, TANN and PLN) and the RTT simulations for the corresponding distance ranges. For both the elastic and acoustic method the decay of the seismic coda following the *S*-wave can be modelled with high precision for lapse times up to 50 s. The onset of the direct *S*-wave in the crust can be modelled with a good agreement in terms of amplitude of the envelope, as well as in terms of shape of the direct pulse using the elastic RTT approach. On the other hand the direct *P*-waves, mainly visible in the radial *L*-component, is more difficult to model. These discrepancies can to a large extent be explained by the isotropic source radiation pattern used in the study, which does not represent the true source radiation. Another reason for the rather poor simulation of the *P*-waves onset is the deviation of the true unknown $Q_i^P/Q_i^S$ ratio to the theoretical value of 2.25 (Shearer 1999), which is assumed in the simulations. Comparisons of the average *S*-peak energies from data and acoustic simulations in general show a good agreement (Fig. 2).

For each event in the four frequency bands, the crustal scattering and absorption parameters are now determined by fitting the envelopes from the elastic and acoustic RTT simulations to the observed envelopes. The fit of all the forward simulations to the reference traces from the 14 events filtered in the four frequency bands is comparable to the fit shown in Fig. 2. The resulting parameters from the elastic and acoustic approach are shown in Fig. 3, the average values of the individually estimated parameters are given in Table 3.

The elastic method yields values from 41 km in the 6 Hz band down to values of 32 km in the 24 Hz band for the absorption path length $l_S^i$. In the acoustic case values for $l_S^i$ vary from 34 km (24 Hz) up to 45 km (6 Hz). Considering the fluctuations of the estimates from the different earthquake, the results obtained from the both methods for the intrinsic attenuation are in good agreement. Deviations of the individual values to the average values are slightly higher in the acoustic approach than in the elastic method (Table 3). In the elastic case the transport mean free path of *S*-waves
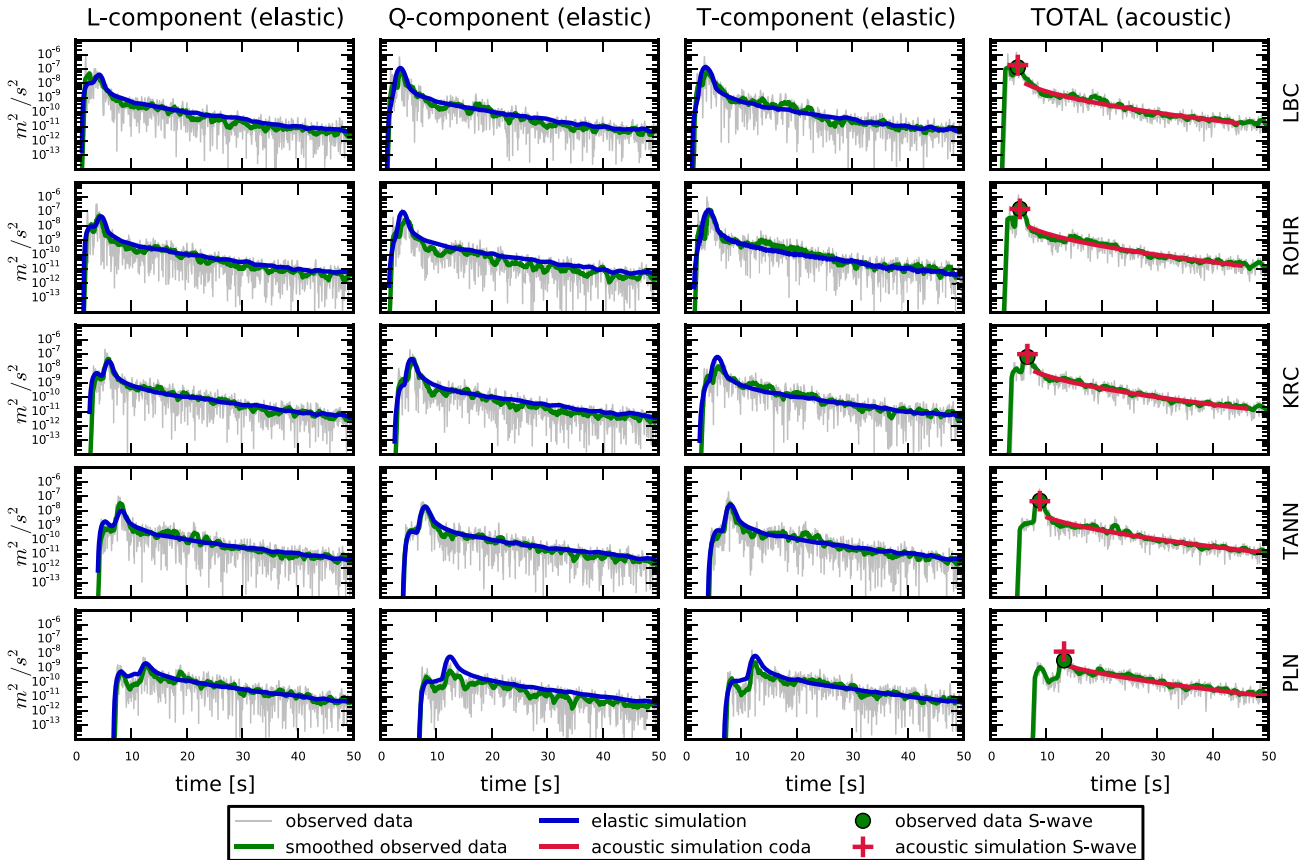
**Figure 2.** Comparison of reference data with elastic and acoustic simulations. This example shows seismic data from earthquake number 10 (see Fig. 1 and Table 1) recorded at stations LBC, ROHR, KRC, TANN and PLN (see Fig. 1 and Table 2). Data are filtered in the 4–8 Hz frequency band ($f_c = 6$ Hz). Thin grey lines represent observed envelopes, green lines represent the smoothed observed envelopes. Columns 1–3 show envelopes for the three components ($L$, $Q$ and $T$) modelled with elastic RTT (blue line). Column 4 contains the total energy envelopes computed with RTT (red line). The mean amplitude of the direct $S$-wave energy for reference and acoustic simulations is represented by the green dot and the red cross, respectively. Units are given in m$^2$/s$^2$.
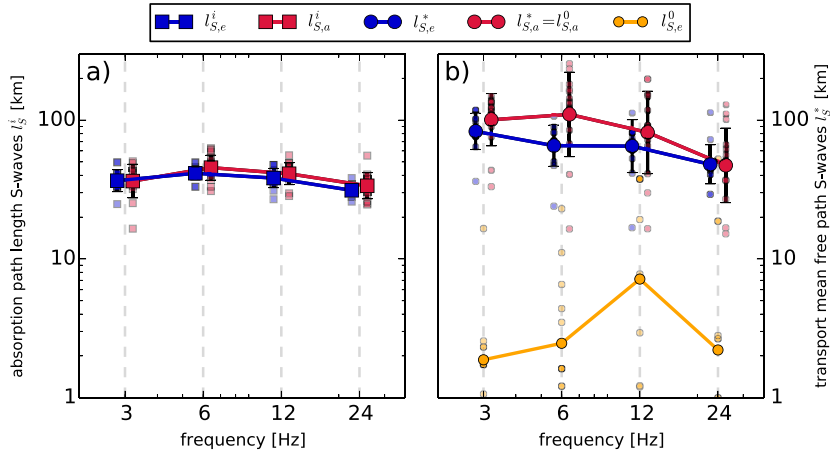


**Figure 3.** Absorption and scattering parameters from elastic and acoustic radiative transfer theory for the four investigated frequency bands. Panel (a) shows the absorption path length for $S$-waves $l_S^i$; panel (b) shows the transport mean free path of $S$-waves $l_S^*$. Blue colour indicates results computed from elastic theory, red colour represents acoustic theory. Symbols in the background indicate the results for each individual earthquake, large symbols represent the geometric mean. In addition to the transport mean free path, the mean free path for $S$-waves estimated from elastic theory $l_{S,e}^0$ is shown in the right side in golden colour. Due to the assumption of isotropic scattering in the acoustic case $l_{S,a}^0$ equals $l_{S,a}^*$. Subscripts $e$ and $a$ denote elastic and acoustic radiative transfer theory, respectively.

$l_S^*$ reaches values from up to 90 km in the 3 Hz frequency band to values of 50 km in the 24 Hz band. The acoustic approximation predicts transport mean free paths for $S$-waves $l_S^*$ of 110 km in the 6 Hz frequency band down to values of 47 km in the 24 Hz

band. The results from both methods again show a good agreement both in terms of absolute values and also in terms of frequency dependence of the parameters, if $g^0$ in the acoustic approximation is interpreted as $g^*$. Again, estimated error bars are smaller in the

**Table 3.** Crustal scattering and intrinsic attenuation parameters in the W-Bohemia/Vogtland region. Quality factors for intrinsic *S*-wave attenuation $Q_i^S$ and *S*-wave scattering attenuation $Q_S^*$ are given in round brackets. Lower and upper numbers indicate the geometric error.

| Frequency [Hz] | $l_S^i$ [km] ($Q_i^S$) | | $l_S^*$ [km] ($Q_*^S$) | |
|---|---|---|---|---|
| | Elastic | Acoustic | Elastic | Acoustic |
| 3 | $38^{+6}_{-5}$ (230) | $36^{+12}_{-9}$ (217) | $90^{+10}_{-9}$ (543) | $101^{+55}_{-35}$ (610) |
| 6 | $41^{+4}_{-4}$ (496) | $45^{+10}_{-8}$ (546) | $66^{+24}_{-18}$ (797) | $110^{+112}_{-55}$ (1329) |
| 12 | $38^{+6}_{-5}$ (919) | $41^{+8}_{-7}$ (992) | $66^{+29}_{-20}$ (1595) | $82^{+80}_{-40}$ (1982) |
| 24 | $32^{+5}_{-3}$ (1538) | $34^{+8}_{-7}$ (1639) | $50^{+14}_{-11}$ (2417) | $47^{+41}_{-22}$ (2272) |

elastic approach (Table 3). Errors in the estimation of the absorption path length using the elastic and acoustic approach are in general smaller than the errors in the estimation of the transport mean free path (Table 3). We note, that scattering and absorption results from the individual earthquakes in some cases show large deviations from the average parameters. Results from solely evaluating the individual earthquakes should therefore not be over-interpreted, rather all results should be interpreted in its entity. From the estimations we conclude, that intrinsic attenuation is dominant in the investigated frequency bands and in the chosen epicentral distances of up to 40 km.

From the estimated values of the transport mean free path in the different frequency bands, information about the ACF describing the random medium can be obtained. Assuming a von Karman type of medium, the Hurst parameter $\kappa$, which describes the roughness of the medium (Sato *et al.* 2012) can be estimated according to following equation:

$$l_S^* \sim f^{2\kappa-1}. \tag{9}$$

Eq. (9) yields following equations for the frequency-dependent elastic and acoustic transport mean free path ($l_{S,e}^*$, $l_{S,a}^*$) from the two methods:

$$l_{S,e}^* = 107 \left(\frac{f}{\text{Hz}}\right)^{-0.24} \text{km}, \tag{10}$$

$$l_{S,a}^* = 178 \left(\frac{f}{\text{Hz}}\right)^{-0.30} \text{km}. \tag{11}$$

Eq. (10) results in a Hurst parameter $\kappa$ of 0.38 for the random medium from the elastic approach, a value of 0.35 for $\kappa$ can be estimated from the acoustic approach (eq. 11). The frequency dependence of the transport mean free path for *S*-waves for both methods with the least square fit is shown in Fig. 4. In the elastic simulations we assumed an exponential ACF of the medium, which
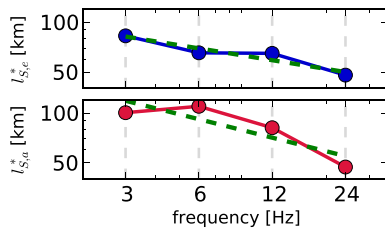
**Figure 4.** Transport mean free path estimates from elastic (top) and acoustic (bottom) simulations for the four investigated frequency bands. Green dashed lines indicate the least-squares fit to obtain the Hurst parameter $\nu$, describing the roughness of the medium (eqs 10 and 11). Subscripts *e* and *a* denote elastic and acoustic RTT, respectively.
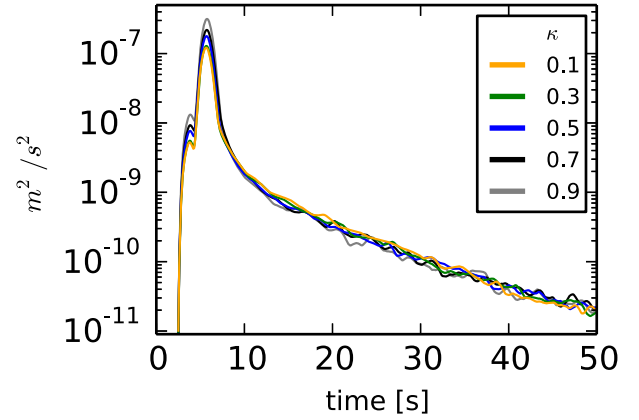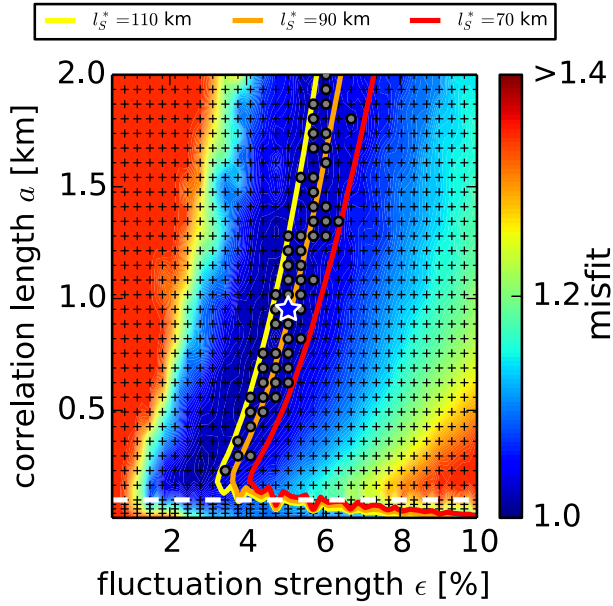
**Figure 5.** Elastic simulations for different types of von Karman medium. Different elastic simulations are shown with a common transport mean free path length for *S*-waves $l_{S,e}^*$ for different values of the Hurst parameter $\kappa$, which defines the roughness of the medium. A value of 0.5 corresponds to an exponential ACF type of medium. Centre frequency of the simulations is 6 Hz. Traces represent the total energy envelopes ($L + Q + T$) recorded at a distance of 18 km.

is a special case of the von Karman type medium with $\kappa = 0.5$. Our estimations of $\kappa$ from both approaches slightly differ from the assumed value of 0.5 for an exponential ACF type medium. We can justify our assumption of an exponential medium by the fact, that different von Karman type medium realizations with equal transport mean free path lengths result in similar seismogram envelopes. This is depicted in Fig. 5, where we show total energy traces ($L + Q + T$) from the elastic simulations in different von Karman type of media with a common transport mean free path length of 90 km at a centre frequency of 6 Hz. In the range of $\kappa$ from 0.1 to 0.5 only small differences in the onsets of the direct *P*- and *S*-wave can be observed. Different assumptions of $\kappa$ in the elastic method will subsequently lead to slightly different values for the transport mean free path in the individual frequency bands. A higher assumed value of $\kappa$ would lead to smaller value of the transport mean free path. Still, the difference between the level of the onsets of the traces for $\kappa = 0.3$ and 0.5 differs only slightly by a factor of below 2 and transport mean free paths do not change significantly. Information about the Hurst parameter $\kappa$ can only be obtained from the frequency dependence of the transport mean free path, which, in the elastic method, is not influenced significantly by the initial choice of the Hurst parameter.

### 5.2 Parameter trade-offs and resolution limits

Additionally to the separation of scattering and intrinsic attenuation, the observed data set is used to investigate the parameter trade-off between fluctuation strength $\epsilon$ and correlation length $a$, as well as to obtain information about the resolution limits of the mean free path of *S*-waves $l_S^0$. The mean free path is a measure of the distance between two scattering events.

We conclude, that it is not possible to individually resolve the parameters $\epsilon$ and $a$. Only the value of the transport mean free path, which results from a combination of these two parameters as a trade-off, can be estimated. This trade-off was already described in earlier studies, see for example Przybilla *et al.* (2009). In this study, the trade-off is demonstrated by comparisons of elastic RTT simulations with observed data, which was already used in Section 5.1. Additional 1020 elastic simulations are computed for different correlation lengths $a$ and fluctuation strengths $\epsilon$. The parameter $a$ is

**Figure 6.** Resolution limits of correlation length $a$ and fluctuation strength $\epsilon$. This figure shows the misfit value for different pairs of correlation length $a$ and fluctuation strength $\epsilon$. Grey crosses represent elastic RTT simulations with different sets of $a$ and $\epsilon$. Intrinsic attenuation $l_S^i$ is constant for all simulations, centre frequency is 6 Hz. The simulation with the lowest misfit is represented by the blue star, grey dots represent simulations with similar misfits. Dashed white line indicates $ak_S = 1$, where $k_S$ represents the $S$-wave number. Simulations below the white line have a value of $ak_S$ smaller than one and are therefore in the wide angle scattering regime. Yellow, orange and red lines represent isolines of the transport mean free paths for 110, 90 and 70 km, respectively. Misfit values are normalized to the smallest misfit value.

uniformly spaced between 0 and 2 km, $\epsilon$ is in the range from 0 to 10 per cent. Intrinsic attenuation is kept constant at a value of $Q_S^i = 600$ to be able to only investigate the effect of scattering attenuation. The centre frequency is 6 Hz, which results in an absorption path length $l_S^i$ of ~50 km. For all different sets of parameters the forward simulations are computed according to Sections 2.1 and 4. Reference envelopes are created from earthquake 10 in the 4–8 Hz frequency band and the misfits to the forward simulations are calculated. The resulting misfit surface for the parameters sets is shown in Fig. 6. A number of simulations with misfits similar to the best simulation can be observed, these simulations are marked with grey dots. In the elastic simulations, some weak fluctuations, especially in the coda window, can be observed. These fluctuations are caused by the limited number of particles used in the simulations and can cause statistical variations that influence the resulting misfit (Gaebler *et al.* 2015). If these variations are taken into account, all simulations marked with grey dots, can explain the data equally well. The shown simulations all have different values for pairs of correlation length $a$ and of fluctuation strength $\epsilon$, but share a similar value for the transport mean free path of $S$-waves $l_S^*$. This is illustrated in Fig. 6, where, additionally to the colour coded misfit, the transport mean free path is illustrated as coloured isolines. The best fitting models all align along similar values of $l_S^*$ ranging from 70 to 100 km. The total energy traces ($L + Q + T$) of these simulations, as well as the total energy reference envelope from station KRC for event 10 in the 4–8 Hz band, are shown in Fig. 7.

The main differences in the traces with a similar transport mean free path length can be observed in the coda following the $S$-wave. These differences are accounted for by fluctuations in the individual
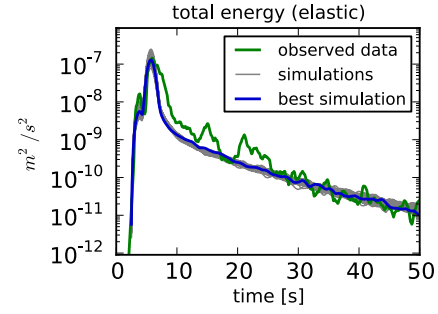


**Figure 7.** Total energy envelopes of smoothed observed data (green line) and best-fitting elastic simulation (blue) for earthquake 10 at station KRC in the 4–8 Hz frequency band. Thin grey lines represent the simulations that can equally well describe the observed seismogram envelopes (Fig. 6).

simulations due to the limited number of particles used. The direct onsets of the $P$- and $S$-wave show only minor differences and are nearly equal for simulations with similar transport mean free path length. From Fig. 6 we conclude, that forward scattering is required to describe the reference data. All simulations with low misfit values have a value of $ak_S$ greater than one, which implies forward scattering. $k_S$ represents the $S$-wave number. Higher misfit values are visible for all simulations with $ak_S$ below one, which would imply wide angle scattering. Even though forward scattering is required, the strength of the forward scattering, described by the value of $ak_S$, cannot be determined. From the elastic and acoustic simulations information about the resolution possibilities of the mean free path of $S$-waves $l_S^0$ can be obtained. In Fig. 3, the estimated values of the mean free path of $S$-waves $l_S^0$ from the elastic method is presented additionally to the transport mean free path. The deviations of $l_S^0$ are in the range from far below 1 km up to 40 km and therefore show much higher uncertainty than $l_S^*$. This fact is also supported by Fig. 8, which shows the misfit values of the simulations already
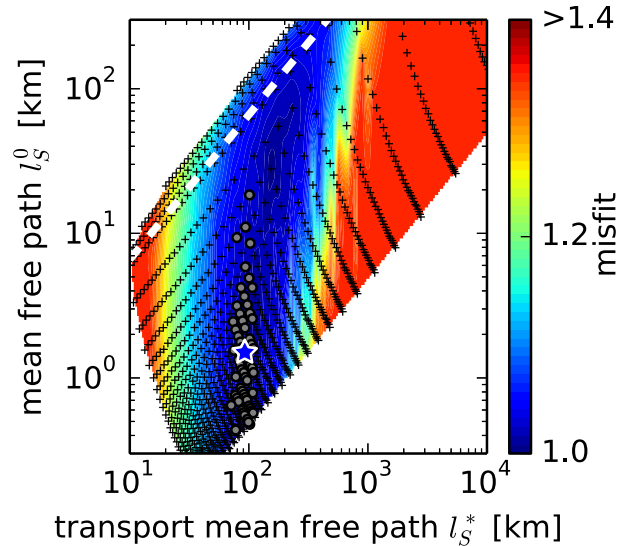


**Figure 8.** Similar to Fig. 6, but for the different pairs of transport mean free path and mean free path. Grey crosses represent elastic RTT simulations. The simulation with the lowest misfit is represented by the blue star, grey dots represent simulations with similar misfits. Dashed white line indicates $ak_S = 1$. Simulations above the white line have a value of $ak_S$ smaller than one and are therefore in the wide angle scattering regime. Misfit values are normalized to the smallest misfit value.

shown in Fig. 6, but for the different values of transport mean free path and mean free path. Note that it is possible to estimate the transport mean free path with a high accuracy and narrow it down to a range of 70 to 110 km. The mean free path, on the other hand, cannot be estimated reliably, as the values from the simulations with low misfits range from a few hundred meters up to over 40 km. There is an upper border for the mean free path $l^0$ given by the transport mean free path $l^*$ ($l^0 < l^*$). This is the case, as $l^0 = l^*$ would imply wide angle scattering rather than forward scattering, which would result in higher misfit values (compare dashed white lines in Figs 6 and 8).

# 6 DISCUSSION

In this study, crustal scattering and intrinsic attenuation parameters are estimated using elastic and acoustic RTT. As the acoustic approach only simulates the propagation of $S$-energy, the focus is on the analysis of the transport mean free path of $S$-waves $l_S^*$ and on the intrinsic attenuation of $S$-waves, expressed through the absorption path length of $S$-waves $l_S^i$. Both methods yield similar results for the scattering and attenuation parameters, with smaller errors estimated in the elastic approach. Both, the elastic and the acoustic theory, yield a similar frequency dependence of the parameters and are able to describe the first onset of the direct $S$-wave as well as the following $S$-wave coda with high precision. The estimated parameters in the different frequency bands are comparable to the results from other studies, but are estimated to be situated in the stronger scattering and intrinsic attenuation regime. The estimated transport mean free path of $S$-waves $l_S^*$ in this study of 47–110 km is comparable to a study by Przybilla *et al.* (2009), who used a local data set in Norway to estimate values of ∼80–170 km for frequencies in the range of 2–10 Hz. A local study by Fielitz & Wegler (2015) estimates absorption path lengths for $S$-waves between 36–43 km for frequencies between 6–24 Hz at the Continental Deep Drilling site in Germany. This is comparable to our estimations of $l_S^i$ in the range of 32–45 km. Investigations of regional data sets in Germany, for example Sens-Schönfelder & Wegler (2006) or Gaebler *et al.* (2015), estimate higher values for the transport mean free path and the intrinsic quality factor for $S$-waves, which indicates weaker intrinsic attenuation and weaker scattering properties. This can be explained by the different penetration depths of the seismic waves for different investigated distance ranges. In the case of regional data sets the direct waves, as well as the scattered energy, sense much deeper regions of the crust in comparison to waves recorded in a local distance range (Calvet & Margerin 2013). Scattering and intrinsic attenuation parameters exhibit a clear depth dependency (Del Pezzo *et al.* 2011) which can explain the different values for the regional and local investigations, even if the study areas are in close proximity.

From the elastic simulations, we infer that it is not possible to estimate the scattering parameters correlation length $a$ and root mean square fractional fluctuations $\epsilon$ separately, but only the transport mean free path of $S$-waves $l_S^*$, which results from a combination the two parameters $a$ and $\epsilon$. This fact can be used to narrow down the parameter space that has to be investigated in inversion or grid search processes. Instead of considering two free scattering parameters ($a$ and $\epsilon$), only the parameter $\epsilon$ is sampled in the parameter finding process. Due to the fact that forward scattering is necessary to explain the data ($ak_S \gg 1$), the parameter $a$ can be fixed in the individual frequency bands, so that $ak_S \gg 1$. Very large values of $a$ result in strong forward scattering, which, in the numeric simulations, would lead to

very long computational times. To avoid this, we suggest to fix the parameter $a$, for example, that $ak_S \sim 6$. As $k_s$ is frequency dependent, different values of $a$ are subsequently required for different frequency bands. Therefore, only considering $\epsilon$ as a free parameter will lead to different values for the transport mean free path and will suffice to give a correct description of the scattering parameters of the medium.

In the acoustic simulations isotropic scattering is assumed, therefore the mean free path $l_S^0$ is equal to the transport mean free path $l_S^*$. From the results of the numeric elastic simulations we conclude, that in the acoustic simulations the transport mean free path $l_S^*$ is measured, the value of the mean free path $l_S^0$ cannot be resolved.

The results from the local data set using acoustic and elastic RTT yield fairly similar values for the $S$-wave scattering and absorption parameters. This indicates that for a simple setup with a half space, isotropic scattering and only modelling $S$-wave propagation, the acoustic approach may suffice to obtain basic parameters about the attenuation properties of the medium. This is especially attractive, as analytic solutions to this approach exist, which can be computed efficiently and deliver results with only minor computational costs. For more complex models however, numerical solutions to the elastic RTEs have to be utilized. This methods includes the possibility of modelling the propagation of $P$- and $S$-energy, as well as conversions between those two modes. The modelling of the two modes of energy allows investigations of the ratio of $Q_i^P/Q_i^S$ and of the ratio $E_P/E_S$ of emitted $P$- to $S$-energy at the source. Furthermore the more realistic assumption of forward scattering can be implemented in the modelling, which results in smaller error bars in the estimation of the scattering and absorption parameters.

# 7 CONCLUSIONS

(1) Intrinsic attenuation and scattering parameters in the W-Bohemia/Vogtland region are estimated using elastic and acoustic RTT. Both methods yield comparable results and a similar frequency dependency of the parameters. In comparison to regional studies in close proximity, the estimated parameters show stronger scattering and intrinsic attenuation. We attribute this fact to the depth dependency of the parameters, as seismic waves recorded on a local or regional scale sense different depths of the crustal structure due to their different penetration depths.

(2) For both intrinsic and scattering attenuation, the elastic simulations show smaller errors in the parameter estimation compared to the acoustic method.

(3) We show from elastic RTT simulations that forward scattering is required to explain the data, however, the amount of forward scattering is not resolvable. The parameters $a$ and $\epsilon$ cannot be resolved individually, but only the transport mean free path can be estimated. For future elastic RTT simulations we suggest to fix the parameter of correlation length $a$, for example, that $ak_s \sim 6$ and only consider $\epsilon$ as a free parameter. This suffices to correctly describe the scattering properties of the medium in form of the resolvable transport mean free path.

(4) For simple model setups, including half space models, isotropic scattering and only simulating the propagation of $S$-energy, the acoustic RTT approach is sufficient, especially as it is computationally efficient. The estimated scattering parameter $l^0$ must be interpreted as transport mean free path $l^*$. However, for the modelling of coupled $P$- and $S$-energy propagation, conversions between those modes, multiple, anisotropic, forward scattering and

complex background models, the numerical elastic RTT approach is essential.

## REFERENCES

Abubakirov, I.R. & Gusev, A.A., 1990. Estimation of scattering properties of lithosphere of Kamchatka based on Monte-Carlo simulation of record envelope of a near earthquake, *Phys. Earth planet. Inter.,* **64,** 52–67.

Aki, K., 1969. Analysis of the seismic coda of local erhquakes as scattered waves, *J. geophys. Res.,* **74**(2), 615–631.

Aki, K., 1980. Attenuation of shear-waves in the lithosphere for frequencies from 0.05 to 25 Hz, *Phys. Earth planet. Inter.,* **21,** 50–60.

Aki, K., 1981. Scattering and attenuation of high-frequency body waves (1–25 Hz) in the lithosphere, *Phys. Earth planet. Inter.,* **26,** 241–243.

Aki, K. & Chouet, B., 1975. Origin of coda waves: source, attenuation, and scattering effects, *J. geophys. Res.,* **80**(23), 3322–3342.

Birch, F., 1961. The velocity of compressional waves in rocks to 10 kilobars, Part 2, *J. geophys. Res.,* **66**(7), 2199–2224.

Calvet, M. & Margerin, L., 2013. Lapse-time dependence of Coda Q: anisotropic multiple-scattering models and application to the pyrenees, *Bull. seism. Soc. Am.,* **103**(3), 1993–2010.

Carolé, E. & Sato, H., 2010. Spatial distribution of scattering loss and intrinsic absorption of short-period S waves in the lithosphere of Japan on the basis of the Multiple Lapse Time Window Analysis of Hi-net data, *Geophys. J. Int.,* **180**(1), 268–290.

Chandrasekhar, S., 1960. *Radiative Transfer,* Dover Publications, Inc.

Dainty, A., Toksöz, M., Anderson, K., Nakamura, Y. & Latham, G., 1974. Seismic scattering and shallow structure of the Moon in Oceanus Procellarum, *The Moon,* **9**(1), 11–29.

Del Pezzo, E., Bianco, F., Marzorati, S., Augliera, P., D'Alema, E. & Massa, M., 2011. Depth-dependent intrinsic and scattering seismic attenuation in north central Italy, *Geophys. J. Int.,* **186**(1), 373–381.

Emoto, K., Sato, H. & Nishimura, J., 2010. Synthesis of vector wave envelopes on the free surface of a random medium for the vertical incidence of a plane wavelet based on the Markov approximation, *J. geophys. Res.,* **115,** B08306, doi:10.1029/2009JB006955.

Fehler, M., Hoshiba, M., Sato, H. & Obara, K., 1992. Separation of scattering and intrinsic attenuation for the Kanto-Tokai region, Japan, using measurements of S-wave energy versus hypocentral distance, *Geophys. J. Int.,* **108**(3), 787–800.

Fielitz, D. & Wegler, U., 2015. Intrinsic and scattering attenuation as derived from fluid induced microseismicity at the german continental deep drilling site, *Geophy. J. Int.,* **201**(3), 1346–1361.

Fischer, T., Horálek, J., Hrubcová, P., Vavryčuk, V., Bräuer, K. & Kämpf, H., 2013. Intra-continental earthquake swarms in West-Bohemia and Vogtland: a review, *Tectonophysics,* **611,** 1–27.

Gaebler, P.J., Sens-Schönfelder, C. & Korn, M., 2015. The influence of crustal scattering on translational and rotational motions in regional and teleseismic coda waves, *Geophys. J. Int.,* **201**(1), 355–371.

Geissler, W.H. *et al.*, 2005. Seismic structure and location of a $CO_2$ source in the upper mantle of the western Eger (Ohře) Rift, central Europe, *Tectonics,* **24**(5), TC5001, doi:10.1029/2004TC001672.

Gusev, A. & Abubakirov, I., 1987. Monte-Carlo simulation of record envelope of a near earthquake, *Phys. Earth planet. Inter.,* **49**(1–2), 30–36.

Heinicke, J., Fischer, T., Gaupp, R., Goetze, J., Koch, U., Konietzky, H. & Stanek, K.-P., 2009. Hydrothermal alteration as a trigger mechanism for earthquake swarms: the Vogtland/NW Bohemia region as a case study, *Geophys. J. Int.,* **178**(1), 1–13.

Hennino, R., Trégourès, N., Shapiro, N., Margerin, L., Campillo, M., van Tiggelen, B. & Weaver, R., 2001. Observation of equipartition of seismic waves, *Phys. Rev. Lett.,* **86**(15), 3447–3450.

Horálek, J., Fischer, T., Boušková, A. & Jedlička, P., 2000. The Western Bohemia/Vogtland region in the light of the WEBNET network, *Stud. Geophys. Geod.,* **44,** 107–125.

Hoshiba, M., 1993. Seperation of scattering attenuation and intrinsic absorption in Japan using the multiple lapse time window analysis of full seismogram envelope, *J. geophys. Res.,* **98,** doi:10.1029/93JB00347.

Lacombe, C., Campillo, M., Paul, A. & Margerin, L., 2003. Separation of intrinsic absorption and scattering attenuation from Lg coda decay in central France using acoustic radiative transfer theory, *Geophy. J. Int.,* **154**(2), 417–425.

Margerin, L., Campillo, M. & van Tiggelen, B., 2000. Monte Carlo simulation of multiple scattering of elastic waves, *J. geophys. Res.,* **105,** 7873–7892.

Paasschens, J., 1997. Solution of the time-dependent Boltzmann equation, *Phys. Rev. E,* **56**(1), 1135–1141.

Prodehl, C., Mueller, S. & Haak, V., 2006. The european cenozoic rift system, in *Continental Rifts: Evolution, Structure, Tectonics,* Vol. 25, pp. 133–212, ed. Olsen, K.H., Elsevier.

Przybilla, J. & Korn, M., 2008. Monte Carlo simulation of radiative energy transfer in continuous elastic random media-three-component envelopes and numerical validation, *Geophy. J. Int.,* **173**(2), 566–576.

Przybilla, J., Korn, M. & Wegler, U., 2006. Radiative transfer of elastic waves versus finite difference simulations in two-dimensional random media, *J. geophys. Res.,* **111**(B4), 1–13.

Przybilla, J., Wegler, U. & Korn, M., 2009. Estimation of crustal scattering parameters with elastic radiative transfer theory, *Geophy. J. Int.,* **178**(2), 1105–1111.

Ryzhik, L., Papanicolaou, G. & Keller, J., 1996. Transport equations for elastic and other waves in random media, *Wave motion,* **24**(4), 327–370.

Sato, H., Fehler, M.C. & Maeda, T., 2012. *Seismic Wave Propagation and Scattering in the Heterogeneous Earth,* 2nd edn, Springer.

Sens-Schönfelder, C. & Wegler, U., 2006. Radiative transfer theory for estimation of the seismic moment, *Geophy. J. Int.,* **167**(3), 1363–1372.

Sens-Schönfelder, C., Margerin, L. & Campillo, M., 2009. Laterally heterogeneous scattering explains Lg blockage in the Pyrenees, *J. geophys. Res.,* **114**(B7), doi:10.1029/2008JB006107.

Shearer, P.M., 1999. *Introduction to Seismology,* Cambridge Univ. Press.

Toksöz, M.N., Dainty, A.M., Reiter, E. & Wu, R.-S., 1988. A model for attenuation and scattering in the Earth's crust, *Pure appl. Geophys.,* **128**(1–2), 81–100.

Trégourès, N., Hennino, R., Lacombe, C., Shapiro, N.M., Margerin, L., Campillo, M. & van Tiggelen, B.A., 2002. Multiple scattering of seismic waves, *Ultrasonics,* **40**(1–8), 269–274.

Turner, J.A. & Weaver, R.L., 1994. Radiative transfer of ultrasound.

Vavryčuk, V., 2011. Detection of high-frequency tensile vibrations of a fault during shear rupturing: observations from the 2008 West Bohemia swarm, *Geophys. J. Int.,* **186**(3), 1404–1414.

Weaver, R., 1990. Diffusivity of ultrasound in polycrystals, *J. Mech. Phys. Solids,* **38,** 55–86.

Wegler, U. & Lühr, B.-G., 2001. Scattering behaviour at Merapi volcano (Java) revealed from an active seismic experiment, *Geophys. J. Int.,* **145**(3), 579–592.

Wegler, U., Korn, M. & Przybilla, J., 2006. Modeling full seismogram envelopes using radiative transfer theory with Born scattering coefficients, *Pure appl. Geophys.,* **163**(2–3), 503–531.

Weinlich, F., Bräuer, K., Kämpf, H. & Strauch, G., 2003. Gas flux and tectonic structure in the western Eger Rift, Karlovy Vary-Oberpfalz and Oberfranken, Bavaria, *Geolines,* **15,** 181–187.

Wessel, P. & Smith, W.H.F., 1991. Free software helps map and display data, *EOS, Trans. Am. geophys. Un.,* **72**(41), 441–441.

Yoshimoto, K., 2000. Monte Carlo simulation of seismogram envelopes in scattering media, *J. geophys. Res.,* **105,** 6153–6161.

Zeis, S., Gajewski, D. & Prodehll, C., 1990. Crustal structure of southern Germany from seismic refraction data, *Tectonophysics,* **176,** 59–86.

Zeng, Y., 1993. Theory of scattered *P*- and *S*-wave energy in a random isotropic scattering medium, *Bull. seism. Soc. Am.,* **83,** 1264–1276.

Zeng, Y., Su, F. & Aki, K., 1991. Scattering wave energy propagation in a random isotropic scattering medium. 1. Theory, *J. geophys. Res.,* **96,** 607–619.